Journal of Alloys and Compounds 1044 (2025) 184463

Contents lists available at ScienceDirect

Journal of Alloys and Compounds

journal homepage: www.elsevier.com/locate/jalcom

Nano-mechanical and chemical analysis of hydrated anodic aluminum oxides

Lydia Daum [a,*], Stefan Ostendorp [a], Martin Peterlechner [a,b], Gerhard Wilde [a]

[a] University of Münster, Institute of Materials Physics, Wilhelm-Klemm-Straße 10, Münster, 48149, Germany
[b] Karlsruher Institute of Technology, Laboratory for Electron Mircoscopy, Engesserstr. 7, Karlsruhe, 76131, Germany

ARTICLE INFO

Keywords:
Aluminum alloys
Anodic aluminum oxide
Hot water sealing
Nanoindentation
Transmission electron microscopy

ABSTRACT

In this work, the effect of various Hot Water Sealing (HWS) times was determined on Anodic Aluminum Oxides (AAOs), that were formed on commercial Al-Mg-Si alloys. The evolving hydroxide layer causes significant alterations to the surface morphology and finishing. A mechanical softening and cracking of the formed aluminum hydroxide (AlOOH) were investigated with nanoindentation and scanning electron microscopy measurements. Cracks form in the vicinity of the surface or precipitates when exposed to sealing conditions commonly used in industry. Additionally, scanning transmission electron microscopy measurements were used to analyze the AlOOH and AAO layers. By analyzing the plasmon energy shift in both phases, electron-energy loss spectroscopy found a continuous transformation of AAO into AlOOH. Based on the nano-mechanical and chemical analyses, a cracking model was proposed. The interaction between AlOOH formation and precipitates incorporated in the AAO mainly contributed to the existence of various networks of cracks.

1. Introduction

The versatile use of Al6xxx (Al-Mg-Si) alloys in industry, compared to pure aluminum (Al), is attributed to the presence of secondary phase particles that enhance key physical properties such as strength-to-weight ratio, formability, and weldability [1–3]. Surface treatments, including the formation of protective coatings, are utilized to improve the durability of aluminum alloys.

In this context, anodic oxidation (anodization) is a prevalent electrochemical process applied to aluminum alloys that forms porous AAOs in acidic solutions [4–6]. Due to the adaptability of an anodization, the formed oxide structure can be precisely controlled by modifying parameters such as electrolyte composition, temperature, applied electric potential and duration. Although anodizing appears to be a straightforward process, the underlying mechanisms governing the formation of porous AAOs are complex and remain partially elusive [5,7–10]. Recently, the chances of a regular pore growth are attributed to a kinetic or diffusional regime [11]. Additionally, the structural integrity of AAOs is highly affected by the anodization behavior of secondary phase particles and solid solution phases in Al alloys [12–15]. Most prominently in Al60xx alloys, voids within the AAO are caused by Si-containing dispersoids [13–15].

Given the porous nature of AAOs, the corrosion resistance was significantly enhanced by closing the pores of the AAO layer. Following that idea, various sealing methods were developed such as HWS, chromate sealing or nickel acetate sealing, among others [16–18]. As chromate or nickel acetate sealing processes produce environmentally harmful byproducts or use toxic chemicals [16], on industrial scales mainly HWS is applied where AAOs coated parts and structures are immersed in boiling water. During this procedure, different phase transformations occur and cause the closure of the pores. These structural changes were investigated with TEM [17], SEM [19], electrochemical impedance spectroscopy (EIS) [20] and X-ray photoelectron spectroscopy [21], among others. Recently, Ono et al. observed a distinct multilayered structure after HWS with TEM measurements. The structural changes might be caused by different diffusion rates for incorporated electrolyte anions, hydroxyl groups and aluminum anions [17]. But most of the mentioned studies focus on pure Al. However, the importance of accounting for the role of precipitates was addressed in a study of anodized and sealed Al5052, Al3003 and Al1050 alloys using SEM and EIS [19]. For sealing times of 20 min, tremendous differences between pure Al and its alloys were observed. Cracks on the surface were assigned to interfacial stresses between the aluminum alloy and the grown AAO [19]. However, in industrial processes a thicker AAO depth is expected which requires longer sealing times than 20 min. For sealing times greater than 1 h, a more comprehensive study of the impact of these longer sealing times on the microstructure evolution is absent so far.

Considering the combination of industry demands and requirements that pose stringent restrictions to materials selection and design also necessitates optimizing complex structures of the (hydro) oxide layer. For

* Corresponding author.
E-mail address: lydiadaum@uni-muenster.de (L. Daum).

https://doi.org/10.1016/j.jallcom.2025.184463
Received 21 May 2025; Received in revised form 14 October 2025; Accepted 15 October 2025
Available online 17 October 2025

this reason, the presence of inert secondary phase particles in the base alloy and the more complex chemical compositions need to be taken into account to understand and describe the formation and subsequent sealing of the oxide layer. Here, a time series of different HWS times is utilized to uncover the intricate and complex processes that govern the transformation into a hydrated AAO layer of a model Al-based alloy with a combination of good mechanical properties, good weldability, and high corrosion resistance. Whereas literature focuses on chemical resistivity measurements with EIS [19] or the fatigue behavior after different amounts of cycling [20], here a systematic analysis regarding the mechanical behavior of the formed aluminum hydroxide is performed with nanoindentation studies. Supporting the observed changes in hardness and embrittlement, a detailed TEM analysis revealed the formation of the hydroxide layer and the impact of precipitates on HWS. While the initial stages of HWS are generating pseudo-boehmite (AlOOH) within the pores [17], chemical differences after prolonged HWS times might suggest rather a reaction-controlled phase transformation of $\mathrm{AAO} \rightarrow \mathrm{pseudo{-}AlOOH} \rightarrow \mathrm{AlOOH}$ instead of diffusion-driven processes at the surface causing the additional growth of AlOOH.

2. Experimental details

2.1. Preparation of hot water sealed samples

Commercially available aluminum alloys (Al6061) were anodized in sulfuric acid with a concentration of 165 g/L using a constant electrolyte temperature of 4 °C. The galvanostatic anodization was performed at a current density of $1.7\,\mathrm{A/dm^2}$. This yielded a porous AAO structure with a targeted thickness of 40 µm and a pore width of approximately 30 nm, mimicking industrial standards.

Afterwards, the aluminum sample was placed in hot boiling water with an additional anti-deposit reagent — Alfiseal. The HWS times ranged from 0.25 to 20 h. The characteristics of all samples were compared to an untreated AAO. The coating and sealing were performed according to MIL-A-8625F, Class III Type 1 Hot Water Sealing specification, for the anodization of aluminum alloys in the diffusional regime of anodization.

An Edwards Auto 306 Physical Vapour Deposition (PVD) operated with an electron beam source was used to coat a conductive layer of 5 nm Cr and 30 nm Au onto the samples after the initial surface characterizations. The vacuum was maintained during the change of the deposition material to decrease possible oxygen contamination. During Au deposition, the pressure was below 3×10^{-6} mbar. The film layer thickness was determined by a quartz crystal balance at the same height as the samples.

A dual beam SEM/FIB Zeiss Crossbeam 340 was used for TEM lamella preparation. A subset of TEM samples was prepared at designated positions, i.e., along the vertices of indents. Additional TEM samples were prepared at arbitrary positions on the surface. All samples were thinned with 30 kV Ga^+ ions until they reached electron transparency. Any amorphous region resulting from the sample preparation was removed in a final polishing step at an ion energy of 5 kV and a beam current of 10 pA.

2.2. Morphology and hardness measurements

All samples were inspected by SEM (FEI Nova NanoSEM 230) using an immersion mode at an electron acceleration voltage of 5 kV to gain a higher amount of collected electrons. Moreover, a deceleration voltage was applied to the sample, leading to an electron energy of 1 keV on the sample's surface to reduce charging effects during image acquisition. Random positions were used to analyze the morphology of prolonged sealed surfaces with respect to crack formation and porosity.

A FemtoTools FT-NMTO4 in-situ SEM nanoindenter was used with a Berkovich tip in displacement mode. By using Continuous Stiffness Measurements (CSM), an array of 20 × 20 indents was created in a crack-free area of each sample. The displacement for each indent was set to reach a depth of 1 µm with a spacing of 10 µm between adjacent indents, thus preventing any accumulation of stress and measuring artifacts. Vickers hardness measurements were performed with a load of 50 gf and a dwell time of 10 s. The indents were placed on arbitrary position on the surface with at least three times of the indent's diameter distance to cracks.

TEM measurements were performed with a C_S-corrected Thermo Fisher Scientific Titan Themis 60–300 microscope equipped with a high brightness field emission gun (XFEG), a monochromator, a quadrupole EDS system, a HAADF detector (Fischione Model 3000), a Gatan Quantum 965 high resolution dual EEL spectrometer and a fast CMOS camera (Ceta 16M, 4k × 4k). The microscope was operated at 3.45 kV extraction voltage and an acceleration voltage of 300 kV. All experiments were performed at cryogenic temperatures with a Gatan Double Tilt Liquid Nitrogen Cooling Holder 636. Cryogenic temperatures and a lower dose rate can reduce the beam damage during data acquisition and prevent measurement-induced artifacts [22–24]. Moreover, each area was only once subjected to either EDS or EELS as multiple measurements can cause dehydration of aluminum hydroxides [25] and structural changes of the alumina [23]. EELS measurements were performed with an electron beam current of 75 pA and DualEELS spectra were obtained with a subpixel-scan to reduce the beam damage.

3. Results and discussion

3.1. Microscopic characterization of the formed oxides

Several SEM images were taken at random positions of the sample to characterize surface roughness, morphology and crack formation after prolonged sealing times. Fig. 1 shows selected SEM images of anodized and sealed surfaces after different HWS times. The unsealed surfaces in Fig. 1(a) and (d) show characteristic features of anodized aluminum alloys such as a distorted structural integrity and a wide range of pore sizes caused by dispersoids and precipitates inside the aluminum matrix [12,13,15]. The surface of the unsealed AAO shows no indication of cracks. The depressions of several hundred nm in size that were observed on the sample surface are chipped off due to mechanical stress release. This is similarly observed for hard anodizations even without a subsequent sealing. Additional x-ray diffraction measurements are displayed in the supplementary material in figure S1. By using identical measurement conditions in between each set, the intensity increase of the amorphous aluminum hydroxide represents the transformation of hydrated alumina.

Sealing the surface for 0.25 h already results in the formation of primary cracks with a width smaller than 1 µm. An apparently constant density of primary cracks is observed after 4 h, as shown in the SEM image in Fig. 1(b). In contrast, the surface morphology exhibits more dense AAO after this sealing process. Now the network of primary cracks is accompanied by secondary cracks, which have a width lower than 200 nm. The distinction between both types is visible in Fig. 1(c). The density of secondary cracks increases with time and does not seem to saturate for the maximally applied sealing time of 20 h. Figure S2(a) of the supplementary material shows the cracked surface of a sealed sample for 16 h. Additional FIB cross-sections are prepared to confirm the nature of both types of cracks. Figure S2(b) and S2(c) show the penetration depth along these cross-sections for primary and secondary cracks. The compact morphology of the hydrated layer suggests an improvement in chemical resistance, whereas the mechanical properties deteriorate. Thus, a more comprehensive analysis of the hydrated alumina is necessary to balance the physical and chemical properties of the protective coating.

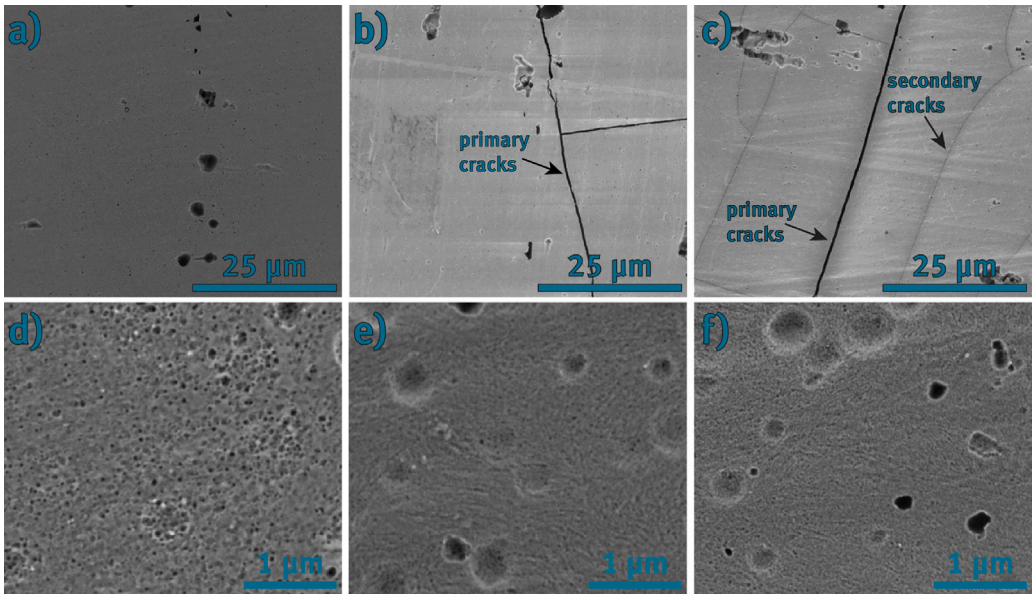

Fig. 1. SEM overview images of anodized Al6061 (a) without HWS, (b) with a HWS time of 4 h and (c) 20 h. The lower magnification SEM images reveal a crack-free morphology in the unsealed condition. Prolonged sealing durations increase the density of primary and secondary cracks as indicated with the arrows. Cracks smaller than 1 µm and 200 nm correspond to primary and secondary cracks, respectively. Higher magnification SEM images of the (d) unsealed surface display a less compact and more open porous AAO structure compared to the sealed counterparts for sealing times of (e) 4 h and (f) 20 h.

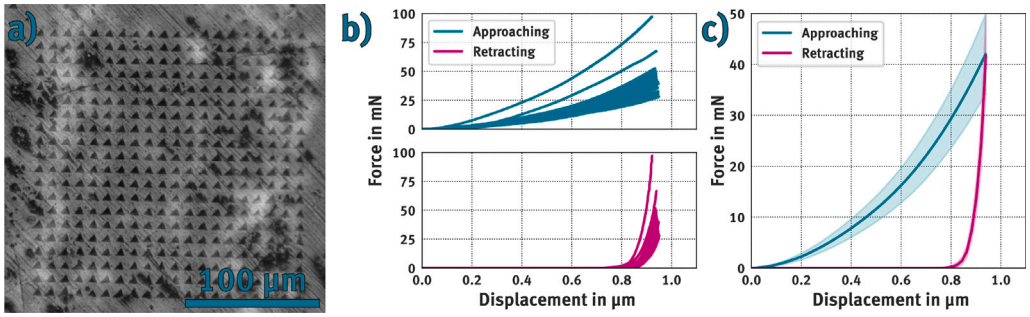

Fig. 2. (a) Nanoindentation array Al6061 after anodization and a HWS time of 20 h. (b) Load–displacement curves of all 400 indents. A Berkovich-tip is used in displacement mode aiming for indentation depths of 1 µm with a spacing of 10 µm. To process the data, the displacement data is split into the approach and retraction movement of the Berkovich tip. (c) The mean and standard deviation of displacement and force are calculated based on the spline of each curve using the python package SCIPY-INTERPOLATE. (For interpretation of the references to color in this figure legend, the reader is referred to the web version of this article.)

3.2. Hardness changes upon HWS

Fig. 2(a) shows a 20 × 20 nanoindentation array after the AAO was sealed in water for 20 h. The measurement satisfies the thin-film criterion of $\frac{h}{t} \rightarrow 0$ concerning indentation depth h and layer thickness t [26]. As it is not possible to polish the surface and given the inherent heterogeneity of AAOs, an averaged load–displacement curve is determined by a *python* script which automatically determines the tip approach and retraction movement. Using the spline of each set, the average force is calculated with the python package SCIPY-INTERPOLATE. The individual and averaged data frame is visualized in Fig. 2(b) for a HWS time of 20 h. Subsequently, the mean of at least 100 individual profiles is computed to analyze the hardness evolution during indentation.

The intended (contact) depth of 1 µm is not achieved, possibly due to elastic recovery after indentation or due to the surface roughness. We can exclude an impact of the material's pile-up since no pile-up is visible in SEM measurements. The surface roughness is thus likely the main cause of the penetration depth variation between the set value and the depth observed after indentation.

Averaged load–displacement curves for the unsealed sample and for three different HWS times are displayed in Fig. 3(a). The maximum displacement of the tip and the resulting maximum force vary for each data set. First, the maximum force is reduced with increasing the HWS time. Secondly, an increased indentation depth is visible for longer HWS times. Both observations might be explained by the existence of an additional aluminum hydroxide layer after HWS. A nanoindentation study between hydrated and anhydrous silicate glasses supports the observations of a reduced hardness for the hydrated compounds [27]. Thus, lower forces are necessary in AlOOH to reach the aimed displacement of the tip. Schneider et al. have shown the impact of hydrogen on the elastic properties of magnetron-sputtered alumina thin films. According to their research, a reduced binding energy of hydroxides as well as a reduction in density resulted in decreased elastic moduli of the alumina hydroxide [28]. Thus, an increase in indentation depth might indicate a reduced elastic recovery.

The averaged hardness along the displacement highlights the change in the mechanical properties after different HWS times as shown in Fig. 3(b). The data sets are divided into two different groups based on their hardness evolution. The first group comprises the unsealed sample in addition to samples which were sealed longer than 12 h. The displayed slopes do not show a strong deviation from an average value characteristic for an indentation depth between 0.2 and 0.8 µm. In contrast, the second group displays a local minimum in hardness during

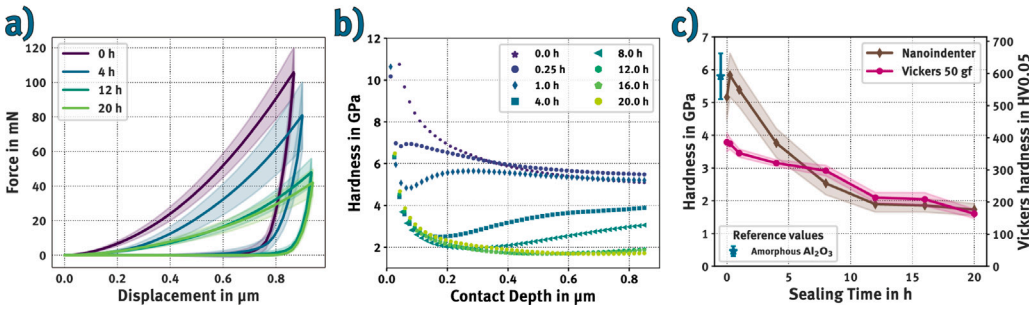

Fig. 3. (a) Averaged load–displacement curves after 0, 4, 12 and 20 h of sealing determined as explained in Fig. 2(b). The shaded area corresponds to the uncertainty of each curve. An increase in HWS time causes a reduction of maximum load during constant displacements of the nanoindenter tip. (b) Hardness development for different HWS times measured in CSM. Hydrated alumina has a significant impact on the hardness of the coating. (c) Comparison between the low-load Vickers and nanoindentation measurements at maximum displacement. The reference value for amorphous anodic Al_2O_3 [29] is in good agreement with the measurement. Especially for thinner layers, Vickers hardness measurements underestimate the hardness.

indentation, likely due to the aforementioned existence of an AlOOH layer. An increase in sealing time results in a thicker AlOOH layer, which is related to the shift of the local hardness minimum to higher displacement values. When the AlOOH layer thickness t is greater than the indentation depth d, the measured hardness corresponds only to the grown AlOOH. Thus, the local minimum vanishes for HWS times greater than 12 h.

Fig. 3(c) summarizes the hardness measured at maximum indentation depth for each sealing time, comparing it to Vickers hardness values measured at a load of 50 gf. Whereas the hardness values align for HWS times exceeding 8 h, the measured Vickers hardness value is below the nanoindentation one for shorter sealing times. This might again be related to the thin-film criterion, where the reduced load of nanoindentation measurements might result in more reliable results for additionally formed thin layers. Literature values for amorphous AAOs [29–31] are in good agreement with the measured value. Using the previously described assumption of a reduced hardness in hydrated materials [27], the subsequent transformation of AAO into AlOOH is observable. Simulations of nanoindentation measurements on porous AAO have demonstrated the influence of indentation depths on the resulting hardness [32]. Their conclusions are based on ≈1 µm thin films of AAO on a glass substrate with a pore diameter of ≈160 nm. While AAO thickness and pore diameter significantly deviate in this work, complex interactions between stress and strain distributions of porous films have to be considered. Especially for the unsealed sample, open pores and a more open surface can result in an underestimation of hardness values when applying nanoindentation. As the hardness increases for HWS times of 0.25 h compared to unsealed AAO, a denser structure of the surface, as proven with SEM images, might lead to a more uniform distribution of the stress and strain during indentation.

3.3. Chemical and structural TEM analysis

To confirm the existence of thin layers of AlOOH, analytical TEM measurements were performed on FIB-prepared cross-sections as exemplified in Fig. 4(a) for a HWS time of 12 h. The extended HWS time caused the formation of a surface layer indicated by the bi-directional arrow. The STEM-HAADF image in Fig. 4(b) reveals the morphology of both layers. While the AAO pore walls remain visible in the lower part of the HAADF image, the upper part appears more dense although a faint AAO structure is still discernible. Given the contrast changes of both layers, the upper part consists of more lighter elements than the lower one. The STEM-BF image in Fig. 4(c) corresponds to the chemical maps obtained with EDS. The line scan perpendicular to the interface shows a more enriched oxygen layer at the top. Given the stoichiometric relation between Al and O in both parts, the EDS measurements support the previous assumption concerning the formation of an AlOOH layer. Incorporated sulfate anions of the electrolyte used during anodization are only detectable in the AAO. A faster migration rate for sulfate anions in AAO was proposed in the literature, despite larger radii of the anion complexes [33]. Recently, the abundance of incorporated sulfate anions was attributed to the ability of the anodization electrolyte and the hot water in HWS to dissolve the anion complexes and migrate them through outward diffusion [17]. While flaky outer layers have been observed in literature [17], the additive used during HWS seems to prevent the formation of such an additional layer.

The interface between these two phases is decorated with voids. Two mechanisms are possible for this occurrence: (1) a nanoscale Kirkendall effect or (2) the release of compressive stresses during HWS.

The traditional Kirkendall effect is based on the occurrence of voids at interfaces caused by unequal atomic diffusion rates in a diffusion couple. Caused by similar processes at the nanoscale, the nanoscale Kirkendall effect causes nanoscale voids. In case of HWS of AAOs, an interface between water and metal oxide is produced. While Al^{3+} ions and incorporated anions are migrating outward during HWS, OH^- ions are moving inward. In order to fulfill the requirements of the nanoscale Kirkendall effect [34–36] and to explain the voids along the interface, the outward migration of metal cations has to be faster than the inward movement to create vacancies along the interface. However, given the pH conditions and temperature of boiling water, the diffusion of cations and anions might not be as strongly affected as required for a pure diffusion-driven void formation process. Furthermore, the diffusion coefficients of Al^{3+}, HSO_4^- and OH^- in water at room temperature are 0.541, 1.385 and 5.273×10^{-9} m^2/s, respectively [37]. As the anion diffusion is approximately an order of magnitude faster than the cation one, it is opposite to the conditions for the Kirkendall effect to occur. The appearance of the nanoscale Kirkendall effect is, to our best knowledge, limited to nanocrystals, whereas the voids observable in this study are decorating large surfaces of amorphous AAO. Moreover, given the amorphous nature of the AAO, classical vacancy-driven diffusion phenomena are not applicable.

Fig. 5(a) shows the AlOOH layer thickness measured by STEM-HAADF images. Each data point is the average of five individual line measurements. The symbol for the second phase at HWS times of 20 h denotes an additional layer between AlOOH and AAO, which was only observed with EDS measurements during that sealing time. Figure S3 in the supplements shows the determination of thinner hydrated alumina layers by using higher magnification TEM images. A linear relationship is observed between AlOOH layer growth and sealing time. This challenges the expected parabolic time dependency of a diffusion-controlled mechanism. Fig. 5(b) displays the growth of an irregular interface between AlOOH and AAO. This interface is highlighted with the dashed line. In the case of a diffusion-controlled mechanism, a constant layer thickness would be expected. Instead, the AlOOH layer thickness varies. This rather suggests an internal restructuring due to

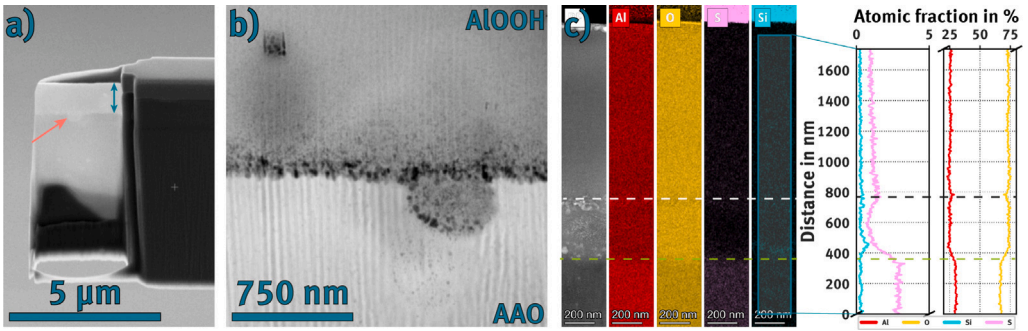

Fig. 4. (a) A FIB cross-section from an Al6061 alloy, anodized and subsequently sealed for 12 h, reveals the existence of an additional surface layer, likely caused by prolonged HWS times. The arrow indicates the position of an oxidized precipitate that was subsequently dissolved during HWS. (b) A STEM-HAADF image of the same lamella shows voids along the interface, which might be attributed to two possible mechanisms: (1) a nanoscale Kirkendall effect or (2) the release of stress at the interface. While the AAO pore walls remain visible in the lower part of the lamella, the upper part appears more compact, although a faint structure is still discernible. (c) A STEM-BF image perpendicular to the interface with corresponding EDS maps and an averaged line scan confirms the depletion of sulphur in the top layer. Moreover, the stoichiometric relation between both parts suggests the formation of AlOOH on top of the AAO.

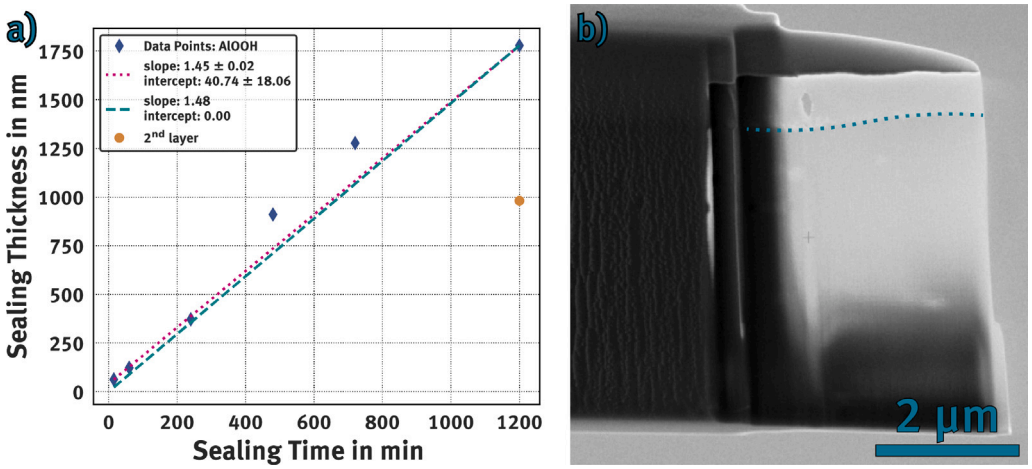

Fig. 5. (a) Layer thickness of AlOOH after different sealing times determined by STEM-HAADF images. Along the lamella, five different lengths are measured and the mean is calculated. The uncertainty of the measurements corresponds to the size of the symbol. Contrary to shorter sealing times, 20 h lead to the formation of a second layer, which is indicated by the additional marker. (b) FIB-lamella of AO61-HWS-8 shows a distorted interface between AAO and AlOOH. Due to varying thicknesses of the newly grown layer, solely diffusion-related mechanisms are excluded in further considerations.

phase transformations of the AAO instead of an additional growth of the AlOOH layer on top of the AAO.

Confirming the hypothesis of a reaction-controlled transformation, STEM-EELS mappings perpendicular to the interface show a gradual conversion from porous AAO to AlOOH in Fig. 6(a). The mentioned regions correspond to areas highlighted in Fig. 6(b), where *Region 1* and *Region 2* are in the completely transformed AlOOH and AAO area, respectively. Each low-loss spectrum is normalized to the plasmon peak in order to analyze the effects of HWS on the binding energies. The feature at ≈8 eV solely appears in the region of the aluminum hydroxide for HWS times exceeding 4 h. This feature is indicated by the existence of red or absence of blue marked regions, respectively, in the mapping of this hydrogen feature within an energy range of (8.6 ± 1.5) eV, as shown in Fig. 2(d). When increasing the HWS time, the AAO region shows a similar behavior than the transformed area in hydroxide layers sealed for shorter times. Given the possibility of determining interband transitions in the area before the plasmon peak, that peak is attributed to the bonding states of O2p and H [25]. This change, visible in Fig. 6(a), confirms the appearance of either AlOOH or $Al(OH)_3$. The expected energies are at (8.1 ± 0.4) and (7.6 ± 0.4) eV, respectively [25,38]. A shift of the plasmon peak caused by an increased electron beam exposure, as reported in literature [25], is excluded as every area was only exposed once to STEM-EELS and every alignment of the beam was done either in vacuum or at the protective Pt layer of the FIB lamella. Additionally, the shift in the plasmon peak maximum might correlate to a change of the electronic structure due to the transformation of aluminum oxide into its hydroxide. The Drude model confirms a shift towards higher energies for Al_2O_3 [25]. However, it is also mentioned that porous structures have an additional effect on the position of the plasmon peak [25]. Given the thickness map of the area in Fig. 6(c), thickness-related artifacts are excluded and a reduced thickness along the interface confirms the existence of voids. In high-temperature oxidation studies, Potter et al. observed sustained hydrogen evolution during linear non-protective magnetite growth, which contributed to embrittlement and void formation [39]. While this study focuses on the hydration of AAOs, a similar mechanism involving hydrogen evolution might play a role in interfacial void formation and might explain the linear growth rate.

Interestingly, longer beam exposures, as required for analytical STEM-EDS, resulted in a smoothing and vanishing of the voids. Beam damage studies of the dehydration of hydrogen in aluminum hydroxides [25] and atomic rearrangements of Al_2O_3 caused by electron beam exposure [23] confirmed a subsequent sputtering of oxygen, which might lead to a re-deposition and filling of voids. In the first case, the oxygen pre-peak observed in the high-loss EELS spectrum suggests rather a formation of unpaired O instead of a formation of O-O bonds during electron beam induced dehydration [25]. As cryogenic temperatures should suppress the pre-peak oxygen formation of $\gamma - Al_2O_3$ [22,

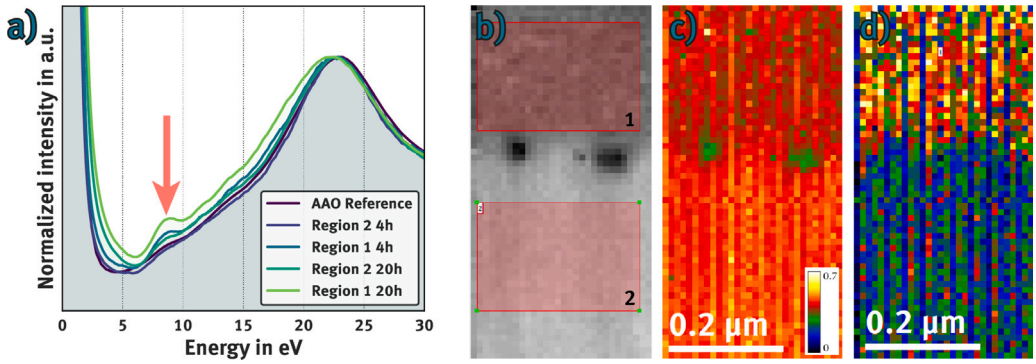

Fig. 6. (a) Excerpt of low loss EELS spectra for various HWS times in different areas indicated in (b). The plasmon peak height is used to normalize each data set for comparison. Each area is only subjected once to the electron beam to prevent any beam damage artifacts. The arrow highlights the feature appearing at higher HWS times. The low-loss spectrum of the reference state is taken of an unsealed AAO of the same material. A marginal shift in plasmon peak energy might indicate the change of the binding energy. The thickness map in (c) shows an average thickness of $\frac{t}{\lambda} = 0.43 \pm 0.05$. Therefore, artifacts resulting from a high deviation in thicknesses are excluded. (d) Map of the hydroxide feature with a higher correlation in the upper region of the measured area. Red regions correlate more with the hydroxide feature than blue regions. (For interpretation of the references to color in this figure legend, the reader is referred to the web version of this article.)

24], the magnitude of the oxygen pre-peak varies significantly in regions of transformed AAO. This indicates that aluminum hydroxides might in fact be more electron beam sensitive than aluminum oxides.

Looking at the remaining mechanism of stress-induced cracking or compression release during HWS, the mechanism might be caused by the volume expansion during the transformation from AAO to AlOOH. Given the chemical reaction of the phase transformation [40]:

$$Al_2O_3 + H_2O \rightarrow 2AlO(OH) \quad (1)$$

$$Al_2O_3 + 3H_2O \rightarrow 2Al(OH)_3 \quad (2)$$

a difference in volume expansion should be expected for the phase transformation. A volume decrease of 25 % was observed for the dehydration of $\gamma - AlOOH$ [41], indicating the existence of compressive stresses during the hydration of Al_2O_3. In the literature, values for the expansion upon AlOOH formation range between 8 and 25 %, depending on the type of oxides formed on the aluminum alloys or pure aluminum [19,42]. Although the mechanism of dehydration is mostly diffusion controlled [41], the shown process might be mainly reaction-controlled by the phase transformation. After the beginning of the phase transformation, voids are forming due to the stresses originating from different volume expansions of Al, AAO and AlOOH. However, localized tensile and shear stresses might occur whenever the expansion is uneven due to an inhomogeneous surface of the AAO. An increase in sealing time will lead to the formation of cracks caused by the volume expansion and embrittlement of the AlOOH layer. Additionally, voids at the interface might decrease the adhesion of the AlOOH layer, which would further result in deteriorated mechanical properties. In general, the existence of a second interface within the AAO might be the origin of secondary cracks after prolonged HWS times.

In 2022, Yanagimoto et al. examined structural changes after HWS within the AAO due to two mechanisms: (1) tensile stresses at the interface between aluminum and AAO and (2) compressive stresses during the formation of hydroxides within cavities of the AAO [19]. Moreover, for other oxide systems, i.e. grown on Si substrates, a similar stress-induced cracking mechanism based on tensile stresses at the interfaces and high compressive stresses within the oxide originating from the hydroxide growth was observed [43]. As the existence of cavities within AAOs depends highly on the anodization behavior of the embedded precipitates [12,13], the magnitude of crack formation will vary significantly when varying the base material for anodization. Given the embrittlement of the oxide, it might be favorable to avoid the formation of a secondary interface by decreasing the HWS time to values ≤1 h.

3.4. Proposed cracking mechanism

The schematic in Fig. 7 comprises the complementary results by nanoindentation, SEM and analytical TEM.

Fig. 7(a) shows the initial structure of AAOs grown on aluminum alloys. Depending on the electrochemical potential of the dispersoids and precipitates, cavities are formed at the interface between dispersoid and AAO. As HWS is performed in boiling water, the difference of the thermal expansion coefficients of the aluminum alloy and AAO are important to consider. Pores are gradually filled with water and transform the AAO into pseudo-AlOOH as indicated in green in Fig. 7(b). Caused by tensile stresses at the interface [43] and compressive stresses within cavities [19], primary cracks are initially formed that penetrate through the oxide layer. The absence of primary cracks on HWS surfaces of AAOs grown on pure aluminum lead to the assumption that the stresses caused by the volume expansion inside the cavities of the oxide are the main cause for crack formation. Fig. 7 (c) shows a possible explanation for the occurrence of primary cracks and highlights the formation of a second interface within the AAO. The purple color shows the tendency of AlOOH to transform the remaining porous layer into an amorphous compact AlOOH structure. However, this additional interface causes mechanical stresses on the remaining AAO which produces voids and cavities along the newly formed interface. Given the stress-related cracking mechanism mentioned before, secondary cracks form again at mechanically weakened regions within the layer. As the hardness decreases drastically for HWS exceeding 4 h, the top layer favors the formation of cracks. Thus, an increase in density of secondary cracks is possible while the density of primary cracks is constant for a given aluminum alloy system.

To confirm this hypothesis of crack formation, different temperatures during sealing or the variation of the composition of aluminum alloys with different precipitates can lead to a more comprehensive overview. Lowering the dose and acceleration voltage in addition to using faster Direct Electron Detector (DED) can result in a more detailed understanding of stress and strain along both interfaces.

4. Conclusions

Processes related to HWS and the impact of precipitates in aluminum alloys were studied by nanoindentation measurements, SEM and TEM analyses. The proposed model for explaining the evolution of the microstructure and the associated mechanical properties builds on prior findings for shorter sealing times [19] and highlights the necessity of balancing the mechanical and chemical properties of AlOOH layers on aluminum alloys.

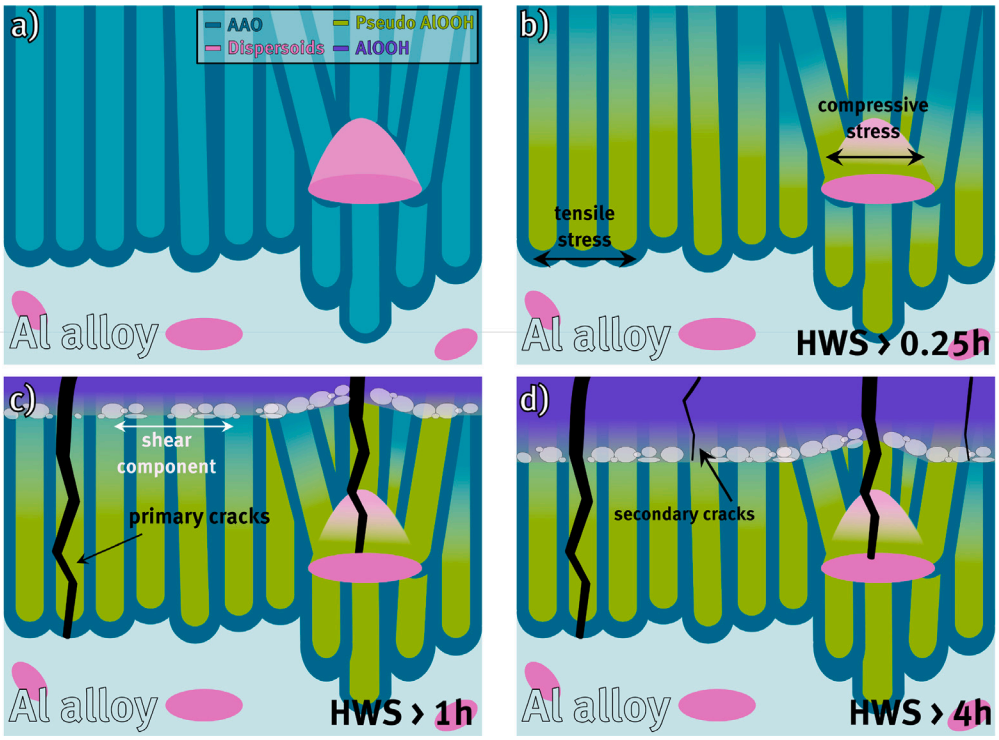

Fig. 7. (a) Schematic of the proposed mechanism of crack formation during prolonged HWS times. AAOs form on the surface of an aluminum alloy with highly distorted pores caused by secondary phases of the alloy. (b) During HWS, the pores are gradually filled with AlOOH. Tensile stresses at the interface and compressive stress within the cavities of precipitates are causing primary cracks already after short sealing times. (c) Increasing the time, a denser AlOOH layer is growing into the AAO. The formation of voids along this second interface indicates the existence of stress. Whenever the stress is greater than a critical value, secondary cracks are formed within the top layer (d). (For interpretation of the references to color in this figure legend, the reader is referred to the web version of this article.)

- Applying prolonged sealing times on AAOs formed on aluminum alloys influences the hardness of the protective coating. Surface-sensitive nanoindentation measurements show a decrease in hardness with increased sealing time. The reduction is correlated to the formation of AlOOH during the HWS process.
- Advanced analytical TEM techniques at cryogenic temperatures indicate a replacement of the formed AAO instead of an additionally grown AlOOH layer. A reaction-controlled phase transformation is suggested to occur at the interface between AlOOH and AAO causing stresses and voids.
- Voids within the AAO, which are caused by secondary phase particles of the aluminum alloy, in addition to different thermal expansion coefficients of the material joining at the two different interfaces are causing two different types of crack formation. While the primary crack formation is linked to the interface between the aluminum alloy and AAO, the much narrower secondary cracks form due to additional stresses at the interface between AlOOH and AAO.
- The crack density of primary cracks saturates after a HWS time of 4 h while the density of secondary cracks grows steadily over the applied HWS time. This is linked to the continuous phase transformation of AAO into AlOOH.
- Although the chemical resistivity might be enhanced with a more dense AlOOH layer, the mechanical properties of the coating are deteriorated. A balance between chemical and mechanical properties is required to obtain application-specific coating characteristics.

CRediT authorship contribution statement

Lydia Daum: Writing – review & editing, Writing – original draft, Visualization, Software, Methodology, Investigation, Formal analysis, Data curation, Conceptualization. **Stefan Ostendorp:** Writing – review & editing, Validation, Supervision, Methodology, Formal analysis. **Martin Peterlechner:** Writing – review & editing, Validation, Supervision, Software, Methodology, Investigation, Formal analysis. **Gerhard Wilde:** Writing – review & editing, Validation, Supervision, Resources, Project administration, Funding acquisition.

Declaration of competing interest

The authors declare the following financial interests/personal relationships which may be considered as potential competing interests: Lydia Daum reports financial support was provided by VAT Group AG. If there are other authors, they declare that they have no known competing financial interests or personal relationships that could have appeared to influence the work reported in this paper.

Acknowledgments

The authors thank VAT Vakuumventile AG, Switzerland for the financial support, close collaboration and for providing the sample material. The DFG is acknowledged for funding our TEM equipment via the Major Research Instrumentation Program, Germany under INST 211/719-1 FUGG.

Appendix A. Supplementary data

Supplementary material related to this article can be found online at https://doi.org/10.1016/j.jallcom.2025.184463.

References

[1] E. Schatzberg, Symbolic culture and technological change: The cultural history of aluminum as an industrial material, Enterp. Soc. 4 (2) (2003) 226–271, http://dx.doi.org/10.1093/es/khg002.

[2] E. Fracchia, F. Gobber, M. Rosso, About weldability and welding of Al alloys: Case study and problem solving, J. Achiev. Mater. Manuf. Eng. 2 (2017) 67–74, http://dx.doi.org/10.5604/01.3001.0010.8036.

[3] W. Chrominski, M. Lewandowska, Precipitation strengthening of Al-Mg-Si alloy subjected to multiple accumulative roll bonding combined with a heat treatment, Mater. Des. 219 (2022) 110813, http://dx.doi.org/10.1016/j.matdes.2022.110813.

[4] F. Keller, M.S. Hunter, D.L. Robinson, Structural features of oxide coatings on aluminum, J. Electrochem. Soc. 100 (9) (1953) 411, http://dx.doi.org/10.1149/1.2781142.

[5] J.P. O'Sullivan, G.C. Wood, N.F. Mott, The morphology and mechanism of formation of porous anodic films on aluminium, Proc. R. Soc. A 317 (1531) (1970) 511–543, http://dx.doi.org/10.1098/rspa.1970.0129.

[6] G.E. Thompson, H. Habazaki, K. Shimizu, M. Sakairi, P. Skeldon, X. Zhou, G.C. Wood, Anodizing of aluminum alloys, Aircr. Eng. Aerosp. Technol. 71 (3) (1999) 228–238.

[7] G.E. Thompson, G.C. Wood, Anodic films on aluminium, in: J.C. SCULLY (Ed.), Treatise on Materials Science and Technology : Corrosion: Aqueous Processes and Passive Films, Vol. 23, Elsevier, 1983, pp. 205–329, http://dx.doi.org/10.1016/B978-0-12-633670-2.50010-3.

[8] J.M. Runge, The Metallurgy of Anodizing Aluminum, Springer International Publishing, Cham, 2018, http://dx.doi.org/10.1007/978-3-319-72177-4.

[9] O. Jessensky, F. Müller, U. Gösele, Self-organized formation of hexagonal pore arrays in anodic alumina, Appl. Phys. Lett. 72 (10) (1998) 1173–1175, http://dx.doi.org/10.1063/1.121004.

[10] G.C. Wood, Sealing anodic oxide films on aluminium, Trans. the IMF 36 (1) (1959) 220–229, http://dx.doi.org/10.1080/00202967.1959.11869791.

[11] I.V. Roslyakov, E.O. Sotnichuk, S.V. Sotnichuk, S.E. Kushnir, K.S. Napolskii, Kinetic and crystallographic control of self-ordering of pores in anodic aluminium oxide, J. Solid State Electrochem. 29 (4) (2025) 1341–1373, http://dx.doi.org/10.1007/s10008-024-06132-w.

[12] F. Keller, G. Wilcox, Anodization of constituent elements, Met. Alloy. 10 (6) (1939) 187.

[13] J. Cote, The behavior of intermetallic compounds in aluminum during sulfuric acid anodizing, part 1: Al-Mn, Al-Fe, Al-Mg2Si, Al-Cr alloys, Plating 4 (1969).

[14] J. Cote, E.E. Howlett, H. Lamb, The behavior of intermetallic compounds in aluminum during sulfuric acid anodizing, part 2, Plating 57 (5) (1970).

[15] L.E. Fratila-Apachitei, H. Terryn, P. Skeldon, G.E. Thompson, J. Duszczyk, L. Katgerman, Influence of substrate microstructure on the growth of anodic oxide layers, Electrochim. Acta 49 (7) (2004) 3169–3177, http://dx.doi.org/10.1016/j.electacta.2003.10.024.

[16] L. Hao, B.R. Cheng, Sealing processes of anodic coatings—past, present, and future, Met. Finish. (2000) 8–18.

[17] S. Ono, H. Asoh, Mechanism of hot water sealing of anodic films formed on aluminum, Corros. Sci. 181 (2021) 109221, http://dx.doi.org/10.1016/j.corsci.2020.109221.

[18] G.E. Thompson, R.C. Furneaux, G.C. Wood, The morphology of sealed anodic films formed on aluminium in phosphoric acid, Trans. the IMF 53 (1) (1975) 97–102.

[19] H. Yanagimoto, K. Saito, H. Takahashi, M. Chiba, Changes in the structure and corrosion protection ability of porous anodic oxide films on pure Al and Al alloys by pore sealing treatment, Mater. (Basel, Switzerland) 15 (23) (2022) http://dx.doi.org/10.3390/ma15238544.

[20] L. Winter, K. Hockauf, T. Lampke, High cycle fatigue behavior of the severely plastically deformed 6082 aluminum alloy with an anodic and plasma electrolytic oxide coating, Surf. Coat. Technol. 349 (2018) http://dx.doi.org/10.1016/j.surfcoat.2018.06.044.

[21] O.J. Murphy, J.S. Wainright, J.J. Lenczewski, J.H. Gibson, M.W. Santana, Spectroscopic investigations of porous and sealed anodic alumina films, J. Electrochem. Soc. 136 (11) (1989) 3518, http://dx.doi.org/10.1149/1.2096497.

[22] H.O. Ayoola, C.-H. Li, S.D. House, C.S. Bonifacio, K. Kisslinger, J. Jinschek, W.A. Saidi, J.C. Yang, Origin and suppression of beam damage-induced oxygen-k edge artifact from g-Al2O3 using cryo-eels, Ultramicroscopy 219 (2020) 113127, http://dx.doi.org/10.1016/j.ultramic.2020.113127.

[23] R. Nakamura, M. Ishimaru, H. Yasuda, H. Nakajima, Atomic rearrangements in amorphous Al2O3 under electron-beam irradiation, J. Appl. Phys. 113 (6) (2013) http://dx.doi.org/10.1063/1.4790705.

[24] A.M. Jasim, X. He, Y. Xing, T.A. White, M.J. Young, Cryo-epdf: Overcoming electron beam damage to study the local atomic structure of amorphous ald aluminum oxide thin films within a tem, ACS Omega 6 (2021) 8986–9000, http://dx.doi.org/10.1021/acsomega.0c06124.

[25] N. Jiang, J.C.H. Spence, In situ eels study of dehydration of $Al(OH)_3$ by electron beam irradiation, Ultramicroscopy 111 (7) (2011) 860–864, http://dx.doi.org/10.1016/j.ultramic.2010.11.004.

[26] Y.-G. Jung, B.R. Lawn, M. Martyniuk, H. Huang, X.Z. Hu, Evaluation of elastic modulus and hardness of thin films by nanoindentation, J. Mater. Res. 19 (10) (2004) 3076–3080, http://dx.doi.org/10.1557/JMR.2004.0380.

[27] D.R. Tadjiev, R.J. Hand, Surface hydration and nanoindentation of silicate glasses, J. Non-Cryst. Solids 356 (2) (2010) 102–108, http://dx.doi.org/10.1016/j.jnoncrysol.2009.10.005.

[28] J.M. Schneider, K. Larsson, J. Lu, E. Olsson, B. Hjörvarsson, Role of hydrogen for the elastic properties of alumina thin films, Appl. Phys. Lett. 80 (7) (2002) 1144–1146, http://dx.doi.org/10.1063/1.1448389.

[29] G. Alcalá, P. Skeldon, G.E. Thompson, A.B. Mann, H. Habazaki, K. Shimizu, Mechanical properties of amorphous anodicalumina and tantala films using nanoindentation, Nanotechnology 13 (2002) 451–455.

[30] S. Ko, D. Lee, S. Jee, H. Park, K. Lee, W. Hwang, Mechanical properties and residual stress in porous anodic alumina structures, Thin Solid Films 515 (4) (2006) 1932–1937, http://dx.doi.org/10.1016/j.tsf.2006.07.169.

[31] P. Nayar, A. Khanna, D. Kabiraj, S. Abhilash, B.D. Beake, Y. Losset, B. Chen, Structural, optical and mechanical properties of amorphous and crystalline alumina thin films, Thin Solid Films 568 (2014) 19–24, http://dx.doi.org/10.1016/j.tsf.2014.07.053.

[32] Z. Hu, M. Shrestha, Q.H. Fan, Nanomechanical characterization of porous anodic aluminum oxide films by nanoindentation, Thin Solid Films 598 (2016) 131–140, http://dx.doi.org/10.1016/j.tsf.2015.11.073.

[33] K. Shimizu, G.M. Brown, H. Habazaki, K. Kobayashi, P. Skeldon, G.E. Thompson, G.C. Wood, Direct evidence for interfacial enrichment of iron during anodic oxide growth on an Al6Fe phase, Corros. Sci. 41 (9) (1999) 1783–1790, http://dx.doi.org/10.1016/S0010-938X(99)00015-3.

[34] Y. Yin, R.M. Rioux, C.K. Erdonmez, S. Hughes, G.A. Somorjai, A.P. Alivisatos, Formation of hollow nanocrystals through the nanoscale Kirkendall effect, Science 304 (5671) (2004) 711–714, http://dx.doi.org/10.1126/science.1096566.

[35] J.G. Railsback, A.C. Johnston-Peck, J. Wang, J.B. Tracy, Size-dependent nanoscale Kirkendall effect during the oxidation of nickel nanoparticles, ACS Nano 4 (4) (2010) 1913–1920, http://dx.doi.org/10.1021/nn901736y.

[36] Z. Wang, L. Pan, H. Hu, S. Zhao, Co9S8 nanotubes synthesized on the basis of nanoscale Kirkendall effect and their magnetic and electrochemical properties, CrystEngComm 12 (6) (2010) 1899–1904, http://dx.doi.org/10.1039/B923206K.

[37] W.M. Haynes, CRC Handbook of Chemistry and Physics, CRC Press, 2011, http://dx.doi.org/10.1201/b17379.

[38] M.P. Prange, X. Zhang, E.S. Ilton, L. Kovarik, M.H. Engelhard, S.N. Kerisit, Electronic response of aluminum-bearing minerals, J. Chem. Phys. 149 (2) (2018) 024502, http://dx.doi.org/10.1063/1.5037104.

[39] E.C. Potter, G.M.W. Mann, The fast linear growth of magnetite on mild steel in high-temperature aqueous conditions, Br. Corros. J. 1 (1) (1965) 26–35, http://dx.doi.org/10.1179/000705965798328182.

[40] K. Wefers, Mechanism of sealing of anodic oxide coatings on aluminium, Aluminium 49 (9) (1973) 622–625.

[41] S.J. Wilson, The dehydration of boehmite, gamma-AlOOH to gamma-Al2O3, J. Solid State Chem. 30 (1979) 247–255.

[42] N. Hu, X. Dong, X. He, J.F. Browning, D.W. Schaefer, Effect of sealing on the morphology of anodized aluminum oxide, Corros. Sci. 97 (2015) 17–24, http://dx.doi.org/10.1016/j.corsci.2015.03.021.

[43] S. Sehr, V. Collier, F. Zok, M.R. Begley, Oxide growth and stress evolution underneath cracked environmental barrier coatings, J. Mech. Phys. Solids 175 (2023) 105275, http://dx.doi.org/10.1016/j.jmps.2023.105275.